OVERLAY

Journal of Theoretical, Computational and Applied Mechanics

JTCAM

DIAMOND OPEN ACCESS

Identifiers
DOI 10.46298/jtcam.12960
DOI 10.5281/zenodo.10581764

History
Received Jan 29, 2024
Accepted May 1, 2024
Published Sept 20, 2024

Associate Editor
Phu Nguyen

Reviewers
Frans van der Meer
Tushar Kanti Mandal

Open Review
HAL hal-04700728

Supplementary Material
See paper's addendum

An implicit staggered algorithm for Crystal Plasticity FEM-based analysis of aluminum

Pedro Areias[1,2], Charles dos Santos[3], Rui Melicio[2,4], and Nuno Silvestre[1,2]

[1] IST – Departament of Mechanical Engineering, Instituto Superior Técnico, Universidade de Lisboa, Lisboa, Portugal
[2] IDMEC – Instituto de Engenharia Mecânica, Lisboa, Portugal
[3] INSA – Institut National des Sciences Appliquées (alumni), Rouen Normandie, France
[4] AEROG – Universidade da Beira Interior, Calçada Fonte do Lameiro, Covilhã, Portugal

In this paper, we propose an implicit staggered algorithm for crystal plasticity finite element method which makes use of dynamic relaxation at the constitutive integration level. An uncoupled version of the constitutive system consists of a multi-surface flow law complemented by an evolution law for the hardening variables. Since a saturation law is adopted for hardening, a sequence of nonlinear iteration followed by a linear system is feasible. To tie the constitutive unknowns, the dynamic relaxation method is adopted. A Green-Nagdhi plasticity model is adopted based on the Hencky strain calculated using a [2/2] Padé approximation. For the incompressible case, the approximation error is calculated exactly. A enhanced-assumed strain element technology is adopted, which was found to be especially suited to localization problems such as the ones resulting from crystal plasticity plane slipping. Analysis of the results shows significant reduction of drift and well defined localization without spurious modes or hourglassing.

Keywords: Green-Naghdi plasticity, CPFEM, multi-surface flow, strongly coupled algorithm, enhanced-assumed strain technology

1 Introduction

Realistic simulations of anisotropy in metal polycrystals require robust single crystal algorithms that consistently produce results within an established error bound. In addition, since polycrystals typically include a large number of grains and significant computational costs, efficiency improvements are a necessity. Fully coupled constitutive systems for single crystals involve a large number of constitutive unknowns (plastic strain tensor, hardening variables, among others) in a nonlinear and frequently nonsmooth system. In a single FCC simulation at one quadrature point, there are at least 18 constitutive unknowns, corresponding to hardening in each of the 12 dominant slip systems plus 6 unknowns corresponding to the flow law (either plastic strain or final stress). Computational costs of the fully coupled constitutive system in a polycrystal are prohibitive for practical applications without considerable computational investment. Staggered algorithms are often used, but naive implementations produce drifting, since there is no measure to reduce the solution error. In that case, both time step and sequence of operations affect the solution (Matthies et al. 2006). A comprehensive description is given by Felippa et al. (2001). In terms of solution classes for the coupled equations, options are as follows:

- Classical full Newton iteration for the coupled constitutive system (e.g. Souza Neto et al. 2008).
- Sequential solution of the constitutive equations, in a staggered form.
- Fixed point iteration with relaxation (e.g. in the fluid-structure interaction context Le Tallec et al. 2001; Küttler et al. 2008).
- Block-Newton partition approach with approximate out-of-diagonal blocks (e.g. Matthies et al. 2003).
- Block-Newton-Krylov where only multiplications are used for the out-of-diagonal blocks Michler et al. 2006.

Effective implicit staggered algorithms have been developed for thermoelasticity (Erbts et al. 2012) and phase-field simulations (Schapira et al. 2023). These are here adopted to improve the accuracy of the staggered algorithm. For FCC (aluminum), we propose an implicit staggered algorithm which strongly couples the solutions (in the sense of Matthies et al. (2006)) to avoid drifting.

Classical works on single crystal plasticity emphasize the strain localization physics and describe the essentials of what is now the Crystal Plasticity Finite Element Method (CPFEM) (Rice 1971; Asaro et al. 1977). Significant developments were achieved to incorporate metallurgical effects in hardening and coupling with grain boundary phenomena (Cailletaud et al. 2003). Current success of algorithms for single crystals can be observed by large-scale polycrystalline ensembles, either combined with homogenization or not. Currently, theoretically sound frameworks exist for single crystal plasticity, including that of Kaiser et al. (2019), where gradient effects in hardening are considered. A review of developments in single crystal plasticity up to the year 2010 was performed by Roters et al. (2010).

This work is organized as follows: in Section 2, a description of the aluminum FCC crystal plasticity is presented, in Section 3 the constitutive integration algorithm for the flow law and the hardening evolution law is presented and a localization test is performed. Section 5 presents the proposed implicit staggered algorithm based on dynamic relaxation, as well as a verification test for its effectiveness. Section 4 presents the finite element technology, specifically a 3D enhanced assumed strain (EAS) hexahedron which is able to capture strain localization. A polycrystal numerical test, following the data of Alankar et al. (2009), is presented in Section 6. In Section 7, conclusions are drawn with respect to the proposed algorithm.

2 Aluminum crystal plasticity

Significant literature exists concerning aluminum plasticity, both in phenomenological (Barlat et al. 1991; Barlat et al. 2005) as well as single crystal (Alankar et al. 2009; Kasemer et al. 2020; Romanova et al. 2022) cases. The FCC dominant slip systems (which is considered here for pure Aluminum) consist of $\{111\}$ planes and $\langle 110\rangle$ directions. Table 1 presents the dominant slip systems which Figure 1 illustrates. The lattice elasticity matrix is anisotropic and reads

$$C = \begin{bmatrix} 106.75 & 60.41 & 60.41 & 0 & 0 & 0 \\ 60.41 & 106.75 & 60.41 & 0 & 0 & 0 \\ 60.41 & 60.41 & 106.75 & 0 & 0 & 0 \\ 0 & 0 & 0 & 28.34 & 0 & 0 \\ 0 & 0 & 0 & 0 & 28.34 & 0 \\ 0 & 0 & 0 & 0 & 0 & 28.34 \end{bmatrix} \times 10^9 \text{ Pa} \tag{1}$$

Table 1 Dominant slip systems of an FCC single crystal.

Slip system	Dense plane ($\boldsymbol{m}_\alpha$)	Dense direction ($\boldsymbol{n}_\alpha$)
1	(111)	$[01\bar{1}]$
2	(111)	$[10\bar{1}]$
3	(111)	$[1\bar{1}0]$
4	$(11\bar{1})$	$[011]$
5	$(11\bar{1})$	$[\bar{1}0\bar{1}]$
6	$(11\bar{1})$	$[\bar{1}10]$
7	$(1\bar{1}1)$	$[011]$
8	$(1\bar{1}1)$	$[\bar{1}01]$
9	$(1\bar{1}1)$	$[\bar{1}\bar{1}0]$
10	$(\bar{1}11)$	$[01\bar{1}]$
11	$(\bar{1}11)$	$[\bar{1}0\bar{1}]$
12	$(\bar{1}11)$	$[\bar{1}\bar{1}0]$

Planes and directions are rotated for the analysis, as Figure 2 shows. The crystal orientation is defined in spherical coordinates using two angles: θ and ϕ. Figure 2 exhibits the transformation.

Figure 1 Dominant slip systems for a FCC crystal.

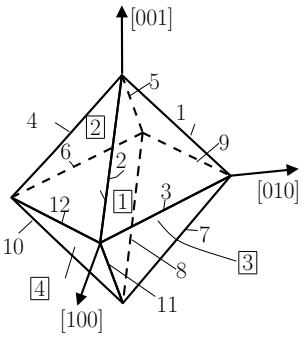

Figure 2 Rotation of the FCC cell in the space x, y, z.

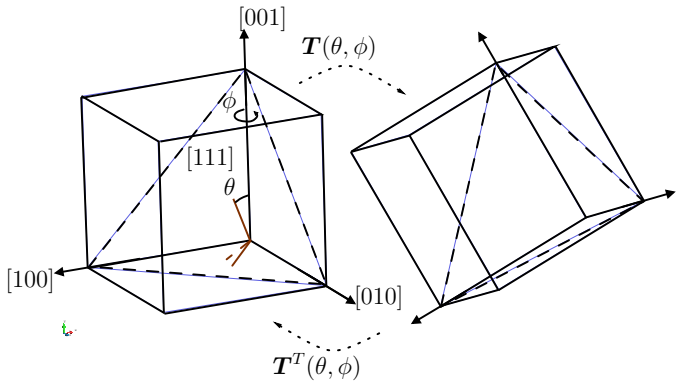

The corresponding transformation matrix defined as

$$\boldsymbol{T}(\theta,\phi) = \begin{bmatrix} \cos\theta\cos\phi & \cos\theta\sin\phi & -\sin\theta \\ -\sin\phi & \cos\phi & 0 \\ \sin\theta\cos\phi & \sin\theta\sin\phi & \cos\theta \end{bmatrix} \tag{2}$$

For the stereographic representation of the loading direction, the transpose of $\boldsymbol{T(\theta,\phi)}$ is adopted. We use a viscoplastic formulation, which is comprised of the following ingredients:

- lattice elastic law,
- additive decomposition of the logarithmic strain into elastic and plastic terms,
- Schmidt flow law,
- hardening laws for the 12 systems.

We adopt the Lagrangian Hencky strain (Schröder et al. 2002)

$$\boldsymbol{\varepsilon} = \frac{1}{2}\log[2\boldsymbol{E} + \boldsymbol{I}] \tag{3}$$

where $\boldsymbol{E}$ is the Green–Lagrange strain and $\boldsymbol{I}$, the identity matrix. Schröder et al. (2002); Shutov et al. (2014); Miehe et al. (2002) have explored the additive decomposition of $\boldsymbol{\varepsilon}$ and the corresponding conjugate stress. For metals, it is a long-standing procedure to adopt a Hooke-like law with the strain (3), see (Anand 1979), which is compatible with hyperelasticity if the Kirchhoff stress is used. The present approach is aligned with the spirit of (Asaro 1983) for the constitutive law. A review is presented by Xiao (2005). Computational origins of the additive strain decomposition in finite strains were established by Papadopoulos et al. (1998); Papadopoulos et al. (2001). The approach inherits some of the formalism adopted in small strain elastoplasticity. In particular, the additive decomposition

$$\boldsymbol{\varepsilon} = \boldsymbol{\varepsilon}_e + \boldsymbol{\varepsilon}_p \tag{4}$$

into elastic $\boldsymbol{\varepsilon}_e$ and plastic $\boldsymbol{\varepsilon}_p$ parts is retained. Theoretical foundations for the use of Equation (4) in finite strains were established by Green et al. (1965) and have been followed by schools of continuum mechanics, see (Lehmann 1991). The lattice elastic law is written as $\boldsymbol{\varepsilon}_e = \mathcal{C}^{-1} : \boldsymbol{\sigma}$. In the isotropic case, Bruhns et al. (2001) proved the satisfaction of the Legendre-Hadamard condition if every principal stretch satisfies $\lambda_k \in [0.21162\ldots, 1.39561\ldots]$ which encompasses the range of elastic behavior of metals discussed by Anand (1979). In Equation (4), the total strain

$\boldsymbol{\varepsilon}$ is assumed to be known from $\boldsymbol{E}$. That allows to establish, in Equation (4), a coupling between the macroscopic stress $\boldsymbol{\sigma}$ and the plastic strain $\boldsymbol{\varepsilon}_p$. The stress for the system α is obtained using Cauchy's lemma

$$\tau^\alpha = \boldsymbol{m}_\alpha \cdot (\boldsymbol{\sigma} \cdot \boldsymbol{n}_\alpha) \Leftrightarrow \tag{5}$$

$$\tau^\alpha = \boldsymbol{M}_\alpha : \boldsymbol{\sigma} \Leftrightarrow \tag{6}$$

$$\tau^\alpha = \boldsymbol{P}_\alpha : (\boldsymbol{\varepsilon} - \boldsymbol{\varepsilon}_p) \tag{7}$$

where $\boldsymbol{P}_\alpha = (\boldsymbol{m}_\alpha \otimes \boldsymbol{n}_\alpha) : C$. The strain rate corresponding to each dominant slip system $\alpha = 1, \ldots, 12$ is introduced as $\dot{\gamma}_\alpha$. The single crystal flow law is provided by the Schmid relation

$$\dot{\boldsymbol{\varepsilon}}_p = \sum_{\alpha=1}^{12} \boldsymbol{M}_\alpha \dot{\gamma}^\alpha \tag{8}$$

known to be an acceptable starting point for FCC crystals and where the flow vector $\boldsymbol{M}_\alpha$ is obtained as $\boldsymbol{M}_\alpha = [\boldsymbol{m}_\alpha \otimes \boldsymbol{n}_\alpha]_{\text{symm}}$. We note that $\boldsymbol{M}_\alpha$ is established for a given crystalline structure, which is fixed during the analysis. Since symmetry ensures that a Voigt form can be established for $\boldsymbol{M}_\alpha$, it becomes possible to write $\boldsymbol{P}_\alpha = \boldsymbol{M}_\alpha : C$. If a fixed yield stress is assumed, then $\xi^\alpha - |\tau^\alpha| \geqslant 0$. Note that in Equation (8) the equivalent strain rate in system α, $\dot{\gamma}^\alpha$ can assume either negative or positive values. It is often assumed that $\dot{\gamma}^\alpha$ follows the viscoplastic law

$$\dot{\gamma}^\alpha = \dot{\gamma}_0^\alpha \left| \frac{\tau^\alpha}{\xi^\alpha} \right|^n \text{sign}[\tau^\alpha]. \tag{9}$$

The hardening law for the critically resolved shear stress ξ^α follows Kasemer et al. (2020) saturation proposal

$$\dot{\xi}^\alpha = h_0 \sum_{\beta=1}^{12} \left[|\dot{\gamma}^\beta| \left(1 - \frac{\xi^\beta}{\xi_\infty^\beta} \right) h_{\alpha\beta} \right] \tag{10}$$

where the coupling matrix is given by Chang et al. (1981) with $q = 1.4$ (Kasemer et al. 2020), see also (Bassani et al. 1991; Zhang et al. 2016):

$$h_{\alpha\beta} = \begin{cases} 1 & \alpha = \beta \\ 1.4 & \alpha \neq \beta. \end{cases} \tag{11}$$

Initial conditions for the previous constitutive system are

$$\boldsymbol{\varepsilon}_p\big|_0 = \boldsymbol{0} \tag{12}$$

$$\xi^\alpha = \xi_0. \tag{13}$$

3 Constitutive integration and testing

Using the backward-Euler integration method between time steps s and $s+1$, Equation (8) reads

$$\boldsymbol{\varepsilon}_{s+1}^p = \boldsymbol{\varepsilon}_s^p + \sum_{\alpha=1}^{12} \boldsymbol{M}_\alpha \Delta\gamma_{s+1}^\alpha. \tag{14}$$

Given Equation (14), the *trial* shear stress for system α is given by $\tau_\alpha^\star = \boldsymbol{P}_\alpha \cdot (\boldsymbol{\varepsilon} - \boldsymbol{\varepsilon}_s^p)$. Trial $\tau_\alpha^\star$ is such that $\tau_\alpha^\star \Delta\gamma_{s+1}^\alpha \geqslant 0$, without sum on α. Integration of Equation (14) for a given time increment Δt is

$$\boldsymbol{\varepsilon}_{s+1}^p - \boldsymbol{\varepsilon}_s^p - \Delta t \sum_{\alpha=1}^{12} \boldsymbol{M}_\alpha \dot{\gamma}_0^\alpha \left| \frac{\boldsymbol{P}_\alpha : (\boldsymbol{\varepsilon} - \boldsymbol{\varepsilon}_{s+1}^p)}{\xi_{s+1}^\alpha} \right|^n \text{sgn}[\tau_\alpha] = \boldsymbol{0}. \tag{15}$$

Newton iteration for $\boldsymbol{\varepsilon}^p_{s+1}$ in Voigt form is performed, which results in a decoupled solution from ξ^α_{s+1}. The Jacobian of (15) is

$$\boldsymbol{J}_{\varepsilon_p} = \boldsymbol{I}_{6\times 6} + \Delta t \sum_{\alpha=1}^{12} \boldsymbol{M}_\alpha \otimes \boldsymbol{P}_\alpha \frac{n\dot\gamma^\alpha_0}{\xi^\alpha_{s+1}} \left| \frac{\boldsymbol{P}_\alpha : (\boldsymbol{\varepsilon} - \boldsymbol{\varepsilon}^p_{s+1})}{\xi^\alpha_{s+1}} \right|^{n-1}. \tag{16}$$

The hardening law is also integrated:

$$\xi^\alpha_{s+1} = \xi^\alpha_s + h_0 \sum_{\beta=1}^{12} \left[|\Delta\gamma^\beta_{s+1}| \left(1 - \frac{\xi^\beta_{s+1}}{\xi^\beta_\infty}\right) h_{\alpha\beta} \right]. \tag{17}$$

Given that Equation (17) is a linear system for ξ^γ_{s+1}, we rewrite it as

$$\xi^\gamma_{s+1}\delta_{\alpha\gamma} = \xi^\alpha_s + h_0 \left[|\Delta\gamma^\beta_{s+1}| \left(1 - \frac{\delta_{\beta\gamma}\xi^\gamma_{s+1}}{\xi^\beta_\infty}\right) h_{\alpha\beta} \right] \tag{18}$$

$$\Leftrightarrow \quad \left(\delta_{\alpha\gamma} + h_0 h_{\alpha\gamma} \frac{|\Delta\gamma^\gamma_{s+1}|}{\xi^\gamma_\infty}\right) \xi^\gamma_{s+1} = \xi^\alpha_s + h_0 |\Delta\gamma^\beta_{s+1}| h_{\alpha\beta} \tag{19}$$

If all slipping systems are active, then it follows that $|\tau_\alpha| - \xi^\alpha_{s+1} = 0$ for $\alpha = 1, \ldots, 12$. Introducing the sign of τ_α as s_α, it follows that $\tau_\alpha - s_\alpha \xi^\alpha_{s+1} = 0$ for active systems. For each α, a summation in $\beta = 1, \ldots, 12$ is required (Einstein summation convention), that is $\tau^\star_\alpha - s_\alpha \xi^\alpha_{s+1} - \boldsymbol{P}_\alpha \cdot \boldsymbol{M}_\beta \Delta\gamma^\beta_{s+1} = \boldsymbol{0}$.

For the sole purpose of calculating $\Delta\gamma^\alpha_{s+1}$, it is convenient to adopt the forward-Euler algorithm for Equation (10), resulting in a linearized version of ξ^α_{s+1}, denominated here as $\xi^{\alpha L}_{s+1} = \xi^\alpha_s + T_{\alpha\beta} s_\beta \Delta\gamma^\beta_{s+1}$ where $T_{\alpha\beta} = h_0 h_{\alpha\beta}(1 - \xi^\beta_s/\xi^\beta_\infty)$ and $s_\beta = \tau_\beta/|\tau_\beta|$. The coupled system, in terms of constitutive unknowns $\{\boldsymbol{\varepsilon}^p_{s+1}; \xi^\alpha_{s+1}, \alpha = 1, \ldots, 12\}$ is written as

$$\boldsymbol{e}_\varepsilon = \boldsymbol{\varepsilon}^p_{s+1} - \boldsymbol{\varepsilon}^p_s - \Delta t \sum_{\alpha=1}^{12} \boldsymbol{M}_\alpha \dot\gamma^\alpha_0 \left| \frac{\boldsymbol{P}_\alpha : (\boldsymbol{\varepsilon} - \boldsymbol{\varepsilon}^p_{s+1})}{\xi^\alpha_{s+1}} \right|^n \operatorname{sgn}[\tau_\alpha] = \boldsymbol{0} \tag{20}$$

$$e_\gamma = \left(\delta_{\alpha\gamma} + h_0 h_{\alpha\gamma} \frac{|\Delta\gamma^\gamma_{s+1}|}{\xi^\gamma_\infty}\right) \xi^\gamma_{s+1} - \xi^\alpha_s - h_0 |\Delta\gamma^\beta_{s+1}| h_{\alpha\beta} = 0; \quad \gamma = 1, \ldots, 12. \tag{21}$$

Concerning the strain measure, we use power-equivalence to obtain a conjugate stress to the Hencky strain. The second Piola-Kirchhoff stress $\boldsymbol{S}$ is power-conjugated to $\dot{\boldsymbol{E}}$ and therefore, in Voigt form,

$$\boldsymbol{S} : \dot{\boldsymbol{E}} = \boldsymbol{\sigma} : \dot{\boldsymbol{\varepsilon}} = \boldsymbol{\sigma} : \frac{\mathrm{d}\boldsymbol{\varepsilon}}{\mathrm{d}\boldsymbol{E}} : \dot{\boldsymbol{E}} \quad \Leftrightarrow \quad \boldsymbol{S} = \boldsymbol{\sigma} : \frac{\mathrm{d}\boldsymbol{\varepsilon}}{\mathrm{d}\boldsymbol{E}}. \tag{22}$$

For moderate strains, the Padé approximation of order $(2, 2)$ is adopted and it is shown to be adequate. The approximation is given by Rezaee-Hajidehi et al. (2021)

$$\log[\boldsymbol{X}] \cong [2/2]_{\log}(\boldsymbol{I} - \boldsymbol{X}) = 3\left(\boldsymbol{X}^2 - \boldsymbol{I}\right)\left(\boldsymbol{X}^2 + 4\boldsymbol{X} + \boldsymbol{I}\right)^{-1}. \tag{23}$$

This ensures the coincidence, at $\boldsymbol{X} = \boldsymbol{I}$, of the approximation and the function up to the third derivative. Popular alternatives to Equation (23) are polynomial approximations with scaling and squaring algorithm (used for the exponential by Sastre et al. (2015)) and the approximation proposed by Bažant (1998). Since $\boldsymbol{\varepsilon} = \frac{1}{2}\log[2\boldsymbol{E} + \boldsymbol{I}]$, we have, in matrix form,

$$\boldsymbol{\varepsilon} \cong 3[\boldsymbol{E}\cdot\boldsymbol{E} + \boldsymbol{E}] \cdot [2\boldsymbol{E}\cdot\boldsymbol{E} + 6\boldsymbol{E} + 3\boldsymbol{I}]^{-1} \tag{24}$$

First and second variations of $\boldsymbol{\varepsilon}$ are required. For the first variation, we have

$$\begin{aligned} \mathrm{d}\boldsymbol{\varepsilon} = {} & 3[\mathrm{d}\boldsymbol{E}\cdot\boldsymbol{E} + \boldsymbol{E}\cdot\mathrm{d}\boldsymbol{E} + \mathrm{d}\boldsymbol{E}] \cdot [2\boldsymbol{E}\cdot\boldsymbol{E} + 6\boldsymbol{E} + 3\boldsymbol{I}]^{-1} \\ & - 3[\boldsymbol{E}\cdot\boldsymbol{E} + \boldsymbol{E}] \cdot [2\boldsymbol{E}\cdot\boldsymbol{E} + 6\boldsymbol{E} + 3\boldsymbol{I}]^{-1} \cdot [2\mathrm{d}\boldsymbol{E}\cdot\boldsymbol{E} + 2\boldsymbol{E}\cdot\mathrm{d}\boldsymbol{E} + 6\mathrm{d}\boldsymbol{E}] \cdot [2\boldsymbol{E}\cdot\boldsymbol{E} + 6\boldsymbol{E} + 3\boldsymbol{I}]^{-1}. \end{aligned} \tag{25}$$

The material tangent modulus, $\mathbb{C}$, is calculated using the chain rule. Using Voigt form, this is calculated as follows:

$$\mathbb{C}_{\text{Voigt}} = \left[\frac{\mathrm{d}\boldsymbol{\varepsilon}}{\mathrm{d}\boldsymbol{E}}\right]^{\top} \cdot \frac{\mathrm{d}\boldsymbol{\sigma}}{\mathrm{d}\boldsymbol{\varepsilon}} \cdot \frac{\mathrm{d}\boldsymbol{\varepsilon}}{\mathrm{d}\boldsymbol{E}} + \boldsymbol{\sigma} \cdot \frac{\mathrm{d}^2\boldsymbol{\varepsilon}}{\mathrm{d}\boldsymbol{E}\mathrm{d}\boldsymbol{E}}. \tag{26}$$

The specific expression for $\mathbb{C}_{\text{Voigt}}$ is too intricate to present in this text. The corresponding Mathematica/Acegen source code is available in the Github repository (Areias 2023). The optimized expression for Equation (26) is compact (around 840 lines of Fortran 95) and dispenses the explicit calculation of the sixth-order tensor $\mathrm{d}^2\boldsymbol{\varepsilon}/\mathrm{d}\boldsymbol{E}\mathrm{d}\boldsymbol{E}$ described in (Miehe et al. 2002). Error analysis by Kenney et al. (1989) presents the following inequality, relating the errors of Padé approximation (after specialization for the present case):

$$\left\| [m/n]_{\log}(-2\boldsymbol{E}) - \log[2\boldsymbol{E} + \boldsymbol{I}] \right\| \leqslant [m/n]_{\log}(2\|\boldsymbol{E}\|) - \log[1 - 2\|\boldsymbol{E}\|] \tag{27}$$

where the right hand side term is denoted $2E^{\max}_{[m/n]\log}$.

This provides an upper bound for the error in $\boldsymbol{\varepsilon}$. Bounds for the condition number are provided in (Kenney et al. 1989). Of course, in the 1D case, the absolute error can be calculated in closed form $E^{1D}_{[m,n]\log} = 1/2|[m/n]_{\log}(2\boldsymbol{E}) - \log[1 + 2\boldsymbol{E}]|$. Quantities $E^{\max}_{[2/2]\log}$ and $E^{1D}_{[2,2]\log}$ are shown in Figure 3. For materials with limited elastic strains, the error in the approximation of logarithm is compatible with current computational mechanics practice. For the incompressible

Figure 3 Upper bound on the error $E^{\max}_{[2/2]\log}$ [solid] compared with the error in closed form $E^{1D}_{[2/2]\log}$ [dashed].

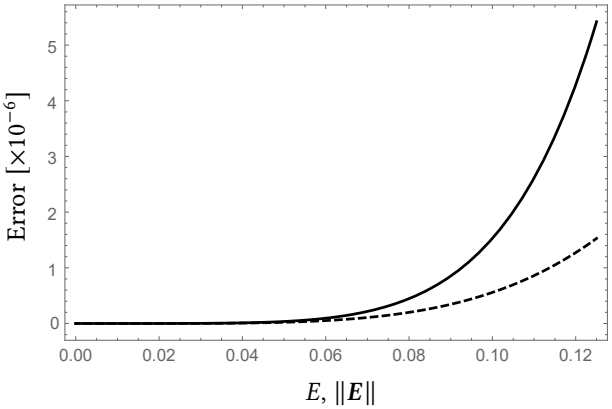

case, which is reasonable in metal plasticity with finite strains, and using principal directions (principal Euler-Lagrange strains E_1, E_2 and E_3), we have, for the Hencky strain,

$$\frac{1}{2}\log[-2\boldsymbol{E}] = \frac{1}{2}\begin{bmatrix} \log[2E_1 + 1] & 0 & 0 \\ 0 & \log[2E_2 + 1] & 0 \\ 0 & 0 & -\log[1 + 2E_1 + 2E_2 + 4E_1E_2] \end{bmatrix} \tag{28}$$

where it was assumed that E_3 is a function of E_1 and E_2:

$$E_3(E_1, E_2) = \frac{1}{2}\left[-1 + \frac{1}{1 + 2E_1 + 2E_2 + 4E_1E_2}\right]. \tag{29}$$

For the $[2/2]$ Padé approximation, we have

$$\boldsymbol{\varepsilon} = \begin{bmatrix} \frac{3E_1(1+E_1)}{3+2E_1(3+E_1)} & 0 & 0 \\ 0 & \frac{3E_2(1+E_2)}{3+2E_2(3+E_2)} & 0 \\ 0 & 0 & \frac{3E_3(1+E_3)}{3+2E_3(3+E_3)} \end{bmatrix}. \tag{30}$$

Figure 4 shows the error $\|1/2\log[2\boldsymbol{E} + \boldsymbol{I}] - \boldsymbol{\varepsilon}\|$ in the domain $E_k \in [-0.25, 0.65]$. It can be observed that even for considerable strains in tension, the error is 0.0258, which corresponds to a relative error of 2.52 %. The calculation of the rotated normals is performed with Kröner/Lee's multiplicative decomposition (Kröner 1960; Lee et al. 1967; Lee 1969) of the deformation gradient $\boldsymbol{F}$ into elastic $\boldsymbol{F}^e$ and plastic parts $\boldsymbol{F}^p$, $\boldsymbol{F} = \boldsymbol{F}^e \cdot \boldsymbol{F}^p$. Since $\boldsymbol{F}$ is determined by the finite element solution, $\boldsymbol{F}_e$ at time step s is determined by the flow law as (Alankar et al. 2009)

$$\boldsymbol{F}^e_s = \boldsymbol{F}_s \cdot [\boldsymbol{F}^p_{s-1}]^{-1} \cdot \left(\boldsymbol{I} - \sum_{\alpha=1}^{12} \boldsymbol{m}_\alpha \otimes \boldsymbol{n}_\alpha \Delta t \dot{\gamma}^\alpha\right) \tag{31}$$

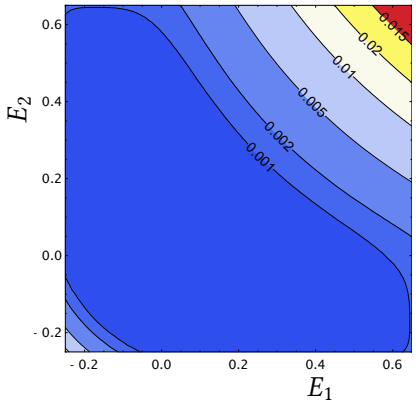

Figure 4 Relative error $E_{[2,2]\log} = \|\frac{1}{2}[2/2]_{\log}(-2\boldsymbol{E}) - \boldsymbol{\varepsilon}\|$ for an incompressible $2D$ problem.

from which the plane normals in the deformed configuration are obtained using the elastic push-forward $\boldsymbol{m}_\alpha^\star = \boldsymbol{F}_s^e \cdot \boldsymbol{m}_\alpha$ (Kaiser et al. 2019). We use the centroidal deformation gradient for purposes of calculating $\boldsymbol{F}_s^e$ and $\boldsymbol{m}_\alpha^\star$. A verification test is performed using the data shown in Figure 5. Two rigid plates are connected to the single crystal. The upper plate is clamped and

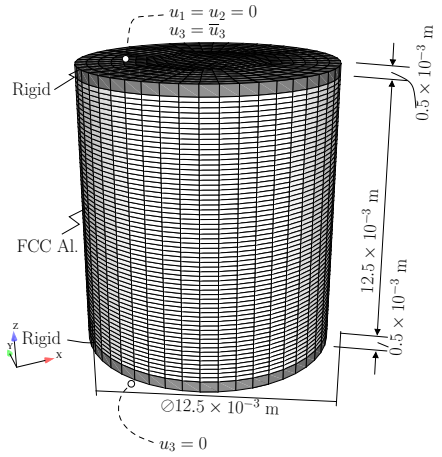

(a) Geometry and boundary conditions. Time increment is $\Delta t = 1 \times 10^{-3}$ s and $\dot{\overline{u}}_3 = 0.001$ m/s.

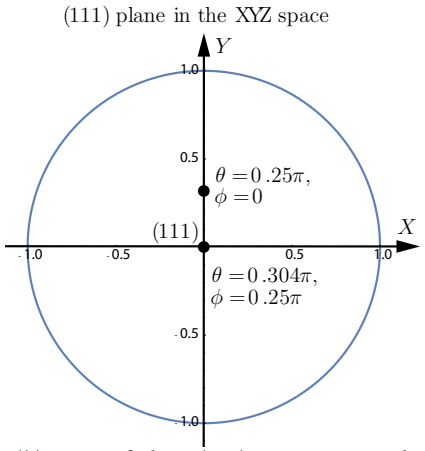

(b) Cases of plane (111) orientation with respect to Z.

Figure 5 Verification test: geometry and boundary conditions for the single crystal cylinder under tension.

pulled in the z direction by an imposed displacement $\overline{u}_3$ where $\dot{\overline{u}}_3 = 0.001$ m/s. The lower plate is fixed in the z direction but left free to have displacement in the $x - y$ plane. We measure the average normal stress $\overline{\sigma}_{33}$ by dividing the reaction force on the z direction. In addition, the average strain, $\overline{E}_{33}$ is obtained as $\overline{E}_{33} = \overline{u}_3/_{12.5\times10^{-3}}$. To force strain localization, we adopt the saturation stress $\xi_\infty^\star$ in Table 2.

$\dot{\gamma}_0$ [s^{-1}]	h_0 [Pa]	ξ_0 [Pa]	ξ_∞ [Pa]	$\xi_\infty^\star$ [Pa]	q	n
0.001	75×10^6	31×10^6	63×10^6	7×10^6	1.4	30

Table 2 Relevant hardening properties for single crystal plasticity of aluminum (Alankar et al. 2009) assumed constant for $\alpha = 1, \ldots, 12$.

Since strain rate dependence is present in the flow law, strain softening is allowed. Localization results for the two orientations are shown in Figure 6 as a function of the element size h (see, e.g. (Hughes 2000) for this nomenclature). The relation between these quantities is represented in Figure 7, where good mesh insensitivity can be observed, especially considering that no regularization is adopted. For $\theta = 0.304\pi$ and $\phi = 0.25\pi$, we show the contour plots of $\xi_1, \ldots, \xi_{12}$ in Figure 8.

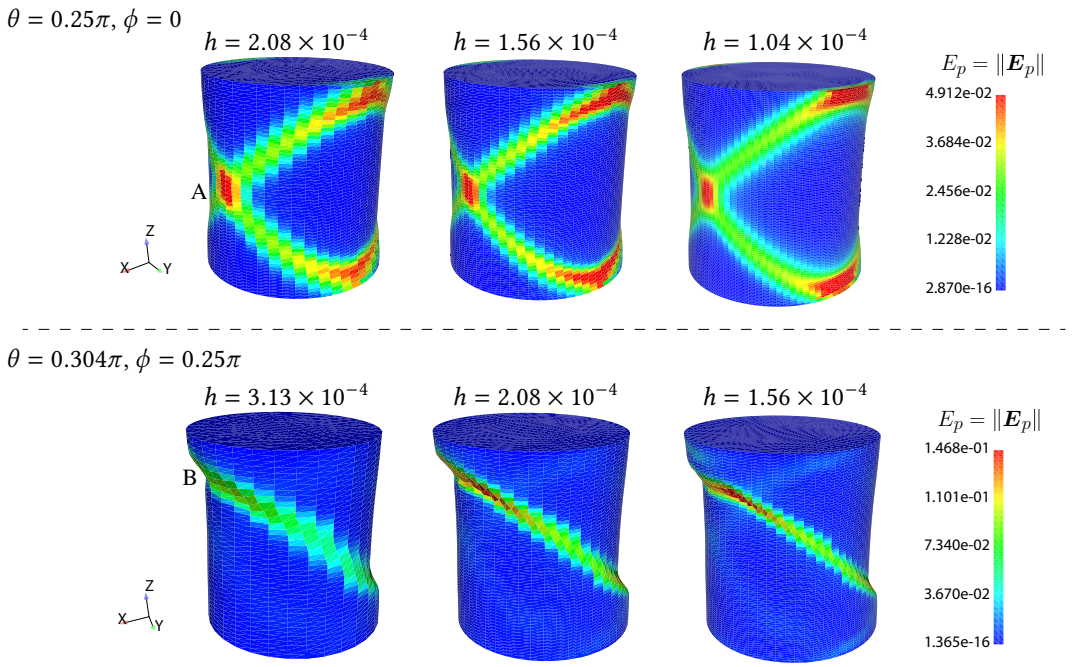

Figure 6 Deformed meshes (10× magnified) and $E_p = \|\boldsymbol{E}_p\|$ contour plots for $\{\theta\}$. Three characteristic mesh sizes $h = 3.13 \times 10^{-4}, 2.08 \times 10^{-4}, 1.56 \times 10^{-4}$ are tested for $\theta = 0.304\pi$ and $\phi = 0.25\pi$ and $h = 2.08 \times 10^{-4}, 1.56 \times 10^{-4}, 1.04 \times 10^{-4}$ for $\theta = 0.25\pi$ and $\phi = 0$. Consistent units are used.

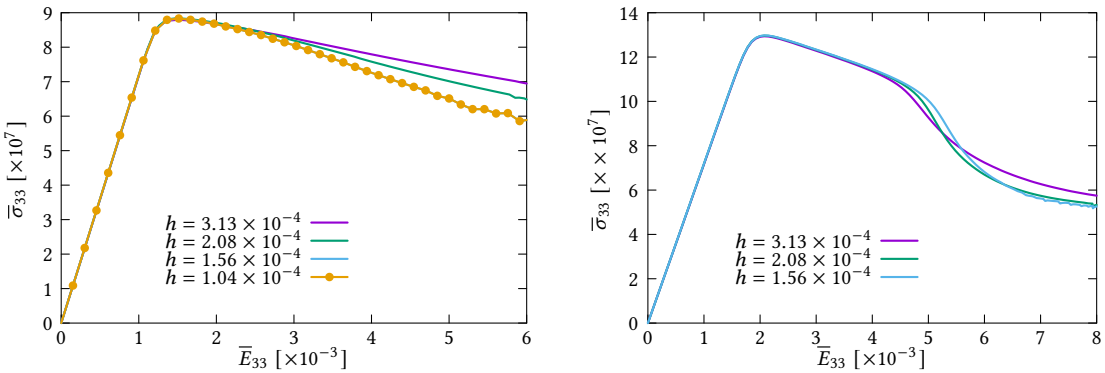

(a) $\theta = 0.25\pi$, $\phi = 0$. **(b)** $\theta = 0.304\pi$, $\phi = 0.25\pi$.

Figure 7 Effect of h on the average stress $\overline{\sigma}_{33}$ and $\overline{E}_{33}$ for two orientations.

4 Finite element formulation

We adopt the 8-node hexahedron with EAS technology developed in (Simo et al. 1990; Simo et al. 1992; Simo et al. 1993), which is appropriate for strain localization problems. A version based on the Green-Lagrange strain was introduced by Andelfinger et al. (1993) and it is employed here. Calculations were performed using Mathematica with the AceGen add-on (Korelc 2002). The classical formalism and the Euler-Lagrange strains (Andelfinger et al. 1993) yields $\boldsymbol{E} = \boldsymbol{E}_u + \boldsymbol{E}_\alpha$. Classical results for $\boldsymbol{E}_u$ and $\boldsymbol{E}_\alpha$ follow:

$$\boldsymbol{E}_u = \frac{1}{2}[\nabla \boldsymbol{u} + \nabla \boldsymbol{u}^\top + \nabla \boldsymbol{u}^\top \cdot \nabla \boldsymbol{u}] \tag{32}$$

$$\boldsymbol{E}_\alpha = \frac{\overline{J}}{J} \overline{\boldsymbol{J}}^{-\top} \cdot \widetilde{\boldsymbol{E}}_\alpha \cdot \overline{\boldsymbol{J}}^{-1} \tag{33}$$

where $[\nabla \boldsymbol{u}]_{ij} = [\partial u_i / \partial X_j]$ is the displacement gradient with respect to the undeformed coordinates and $\widetilde{\boldsymbol{E}}_\alpha$ is the enhanced strain in parent-domain coordinates (Simo et al. 1993). It is required to adopt the centroidal Jacobian matrix $\overline{\boldsymbol{J}}$ and the corresponding determinant $\overline{J}$ to ensure the patch-test satisfaction. The EAS modes are based on the interpolation of the bending deformation modes. 12 additional, internal element degrees-of-freedom are adopted, which here we denote by

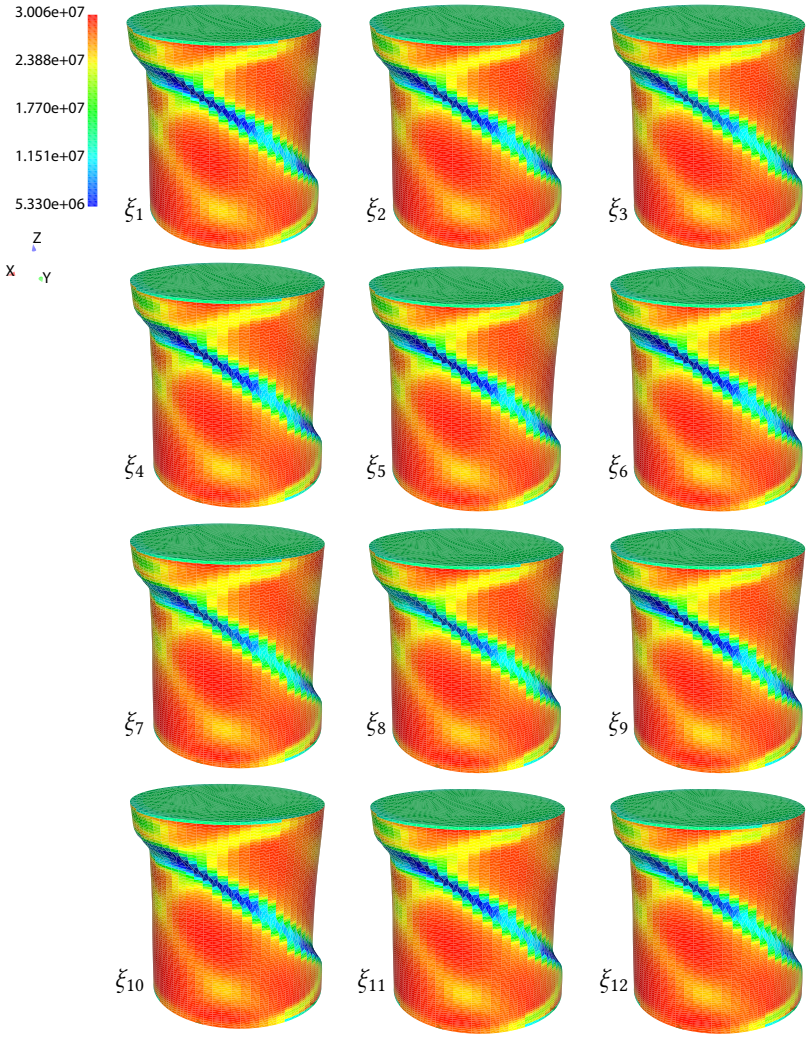

Figure 8 Contour plots of $\xi_1, \ldots, \xi_{12}$ for $\theta = 0.304\pi$ and $\phi = 0.25\pi$.

the letter $\boldsymbol{\alpha} = \{\alpha_1, \ldots, \alpha_{12}\}$. Using Voigt form (Belytschko et al. 2000), it follows that

$$\widetilde{\boldsymbol{E}}_{\alpha}^{\text{voigt}} = \begin{bmatrix} \xi_2 & \xi_3 & \xi_2\xi_3 & 0 & 0 & 0 & 0 & 0 & 0 & 0 & 0 & 0 \\ 0 & 0 & 0 & \xi_1 & \xi_3 & \xi_1\xi_3 & 0 & 0 & 0 & 0 & 0 & 0 \\ 0 & 0 & 0 & 0 & 0 & 0 & \xi_1 & \xi_2 & \xi_1\xi_2 & 0 & 0 & 0 \\ 0 & 0 & 0 & 0 & 0 & 0 & 0 & 0 & 0 & \xi_3 & 0 & 0 \\ 0 & 0 & 0 & 0 & 0 & 0 & 0 & 0 & 0 & 0 & \xi_2 & 0 \\ 0 & 0 & 0 & 0 & 0 & 0 & 0 & 0 & 0 & 0 & 0 & \xi_1 \end{bmatrix} \begin{pmatrix} \alpha_1 \\ \vdots \\ \alpha_{12} \end{pmatrix}. \tag{34}$$

As mentioned, patch test is satisfied a-priori by the the use of $\overline{J}$ and $\overline{\boldsymbol{J}}$ in Equation (33) (Simo et al. 1992; Simo et al. 1993). Using the undeformed configuration, the full weak form corresponding to the decomposition is

$$\underbrace{\int_{\Omega_0} \boldsymbol{S} : (\delta \boldsymbol{E}_u + \delta \boldsymbol{E}_\alpha) \mathrm{d}V}_{\delta W_{\text{int}}} = \underbrace{\int_{\Omega_0} \rho_0 \overline{B} \cdot \delta \boldsymbol{u} \mathrm{d}V + \int_{\partial\Omega_0} \overline{\boldsymbol{T}} \cdot \delta \boldsymbol{u} \mathrm{d}A}_{\delta W_{\text{ext}}} \tag{35}$$

where the Piola stress vector $\overline{\boldsymbol{T}}$, resulting from integration by parts, is calculated as (Wriggers 2008) $\overline{\boldsymbol{T}} = \boldsymbol{F} \cdot \boldsymbol{S} \cdot \boldsymbol{N}$ where $\boldsymbol{F}$ is the deformation gradient and $\boldsymbol{N}$ is the outer normal to $\partial\Omega_0$. The second Piola-Kirchhoff stress $\boldsymbol{S}$ is a function of the total Green-Lagrange strain $\boldsymbol{E}$ as $\boldsymbol{S} \equiv \boldsymbol{S}(\boldsymbol{E}_u + \boldsymbol{E}_\alpha)$. Use of Newton iteration for Equation (35) requires the calculation of the variation

$$\Delta_u \delta W_{\text{int}} \cdot \Delta \boldsymbol{u} + \Delta_\alpha \delta W_{\text{int}} \cdot \Delta \boldsymbol{\alpha} = \delta W_{\text{ext}} - \delta W_{\text{int}} \tag{36}$$

in both hand-sides, assuming that $\Delta_u \delta W_{\text{ext}} = 0$. The source code for this element (forces and tangent stiffness) is available on Github Areias 2024a. It is worth noting that a development of EAS has been used with single crystal plasticity by Fohrmeister et al. (2019).

5 Implicit staggered algorithm

Since a decoupled constitutive system, Equations (20) and (21), is solved, corresponding to the flow law and the hardening evolution, explicit algorithms produce drift, as is the case in thermoelasticity (Erbts et al. 2012), fluid-structure interaction (Küttler et al. 2008; Degroote et al. 2010) and phase-field simulations (Schapira et al. 2023). The study by Erbts and Düster shows that dynamic relaxation with appropriate predictors produces efficient and stable results to remove the drift. We adopt dynamic relaxation and introduce a substep index i as a superscript. Hardening variables $\boldsymbol{\xi}$ are adopted in the relaxation. Index interpretation on $\boldsymbol{\xi}_s^i$ is substep i of time step s. Since the value of $\boldsymbol{\xi}$ depends on $\Delta\boldsymbol{\gamma}$ and this also depends on $\boldsymbol{\xi}$, the staggered solution must comply with the original coupled system. To represent these dependencies, we introduce the operator $\Xi_\star(\boldsymbol{\xi})$ as (see (Erbts et al. 2012, Eq. (28)) for a similar operator)

$$\widetilde{\boldsymbol{\xi}}_{s+1}^{i+1} \leftarrow \Xi_\star(\boldsymbol{\xi}_{s+1}^i) = \Xi[\Delta\boldsymbol{\gamma}, \boldsymbol{\xi}_{s+1}^i] \quad \text{where} \quad \Delta\boldsymbol{\gamma} \equiv \Gamma(\boldsymbol{\xi}_{s+1}^i). \tag{37}$$

Relaxation methods make use of a combination of fixed-point iteration with heuristic acceleration. The hardening variable residual for substep $i+1$ is given by

$$\boldsymbol{r}_{i+1} \leftarrow \widetilde{\boldsymbol{\xi}}_{s+1}^{i+1} - \boldsymbol{\xi}_{s+1}^i \tag{38}$$

Updating is based on linear combination of the image (37) and the previous substep:

$$\boldsymbol{\xi}_{s+1}^{i+1} \leftarrow (1-\omega_i)\boldsymbol{\xi}_{s+1}^i + \omega_i \widetilde{\boldsymbol{\xi}}_{s+1}^{i+1} \tag{39}$$

where ω_i is the coefficient of the linear combination, $\omega_i \in]0, 2[$. Heuristics for updating ω_i have been discussed at length. We here follow (Erbts et al. 2012):

$$\omega_{i+1} \leftarrow \omega_i \left[1 + \frac{(\boldsymbol{r}_i - \boldsymbol{r}_{i+1}) \cdot \boldsymbol{r}_{i+1}}{(\boldsymbol{r}_i - \boldsymbol{r}_{i+1}) \cdot (\boldsymbol{r}_i - \boldsymbol{r}_{i+1})}\right]. \tag{40}$$

Algorithm 1 is adopted in our code.

$\varepsilon \leftarrow 10^{-5}$
$\boldsymbol{\xi}_{s+1}^0 \leftarrow \boldsymbol{\xi}_s$
Newton iteration: $\Delta\boldsymbol{\gamma} \leftarrow \Gamma(\boldsymbol{\xi}_{s+1}^0)$
Linear solution: $\widetilde{\boldsymbol{\xi}}_{s+1}^1 \leftarrow \Xi[\Delta\boldsymbol{\gamma}, \boldsymbol{\xi}_{s+1}^0]$
Initial substep residual: $\boldsymbol{r}_0 \leftarrow \widetilde{\boldsymbol{\xi}}_{s+1}^1 - \boldsymbol{\xi}_{s+1}^0$
Initial coefficient: $\omega_0 \leftarrow 1/2$
Estimate $\boldsymbol{\xi}_{s+1}^1 \leftarrow (1-\omega_0)\boldsymbol{\xi}_{s+1}^0 + \omega_0 \widetilde{\boldsymbol{\xi}}_{s+1}^1$
$i \leftarrow 0$
while $\|\boldsymbol{r}_i\| \geqslant \varepsilon \|\boldsymbol{r}_0\|$ **do**
    $\widetilde{\boldsymbol{\xi}}_{s+1}^{i+2} \leftarrow \Xi_\star(\boldsymbol{\xi}_{s+1}^{i+1})$
    $\boldsymbol{r}_{i+1} \leftarrow \widetilde{\boldsymbol{\xi}}_{s+1}^{i+2} - \boldsymbol{\xi}_{s+1}^{i+1}$
    $\omega_{i+1} \leftarrow \omega_i [1 + \frac{(\boldsymbol{r}_i - \boldsymbol{r}_{i+1}) \cdot \boldsymbol{r}_{i+1}}{(\boldsymbol{r}_i - \boldsymbol{r}_{i+1}) \cdot (\boldsymbol{r}_i - \boldsymbol{r}_{i+1})}]$
    $\boldsymbol{\xi}_{s+1}^{i+2} \leftarrow (1-\omega_{i+1})\boldsymbol{\xi}_{s+1}^{i+1} + \omega_{i+1} \widetilde{\boldsymbol{\xi}}_{s+1}^{i+2}$
    $i \leftarrow i+1$
end while

Algorithm 1 Dynamic relaxation algorithm for $\Delta\boldsymbol{\gamma}$ and $\boldsymbol{\xi}$.

The effect of time step size Δt in the drifting is assessed in Figure 9. The uncoupled version is run with two successive passes for $\Delta\boldsymbol{\gamma}$ and $\boldsymbol{\xi}_{s+1}$ and this is compared with Algorithm 1. The algorithm is inserted in our in-house code SimPlas (Areias 2024b) and combined with the existing finite element technology.

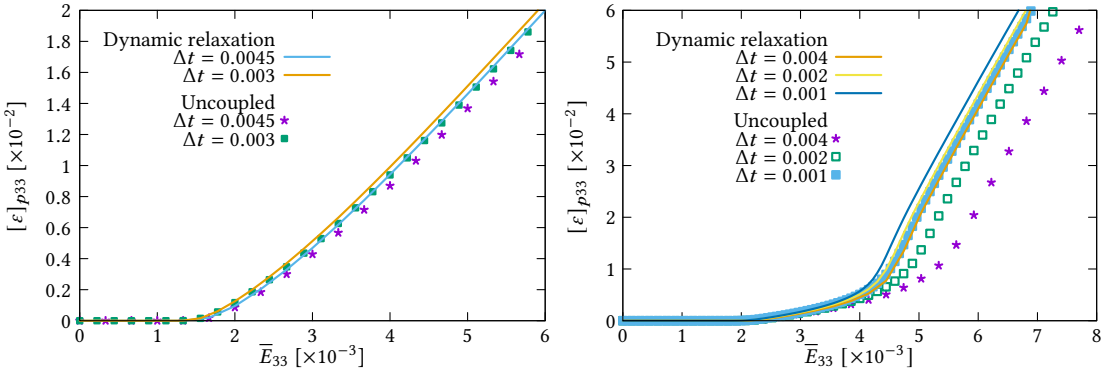

(a) $\theta = 0.25\pi$, $\phi = 0$ at point A. **(b)** $\theta = 0.304\pi$, $\phi = 0.25\pi$ at point B.

Figure 9 Effect of dynamic relaxation on $[\varepsilon_p]_{33}$ for single crystal FCC.

6 Numerical assessment

We now test a polycrystalline rectangular cuboid as depicted in Figure 10. The initial distribution of (111) plane in the XYZ space is shown in Figure 10(b). This test was proposed by Alankar et al.

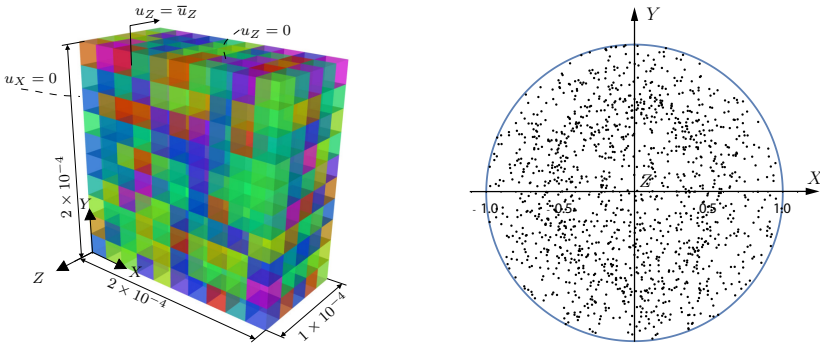

(a) Geometry and boundary conditions. **(b)** Distribution of (111) planes.

Figure 10 Aluminum polycrystal in the undeformed configuration.

(2009). In contrast with that reference, a free edge with $X = 2 \times 10^{-4}$ is left to exhibit the texture. The contour plots of ξ_k and $E_p = \|\boldsymbol{E}_p\|$ for 80 % compression are shown in Figure 11. These are close to those reported in (Alankar et al. 2009) but the right edge $X = 2 \times 10^{-4}$ is here left free.

Texture evolution is shown in Figure 12 and is similar to that published by Alankar et al. (2009), who used slightly different boundary conditions. We now assess drifting of $\xi_1, \ldots, \xi_{12}$. For conciseness reasons, Figure 13 shows the evolution of ξ_1, ξ_5, ξ_6, ξ_7, ξ_9 and ξ_{12} using the classical staggered algorithm and dynamic relaxation. Two time-steps are tested: $\Delta t = 0.0025$ s and $\Delta t = 0.0075$ s. If the traditional staggered decomposition is adopted, with all variables, for the larger time-step, at a compression value of 55 %, drifting occurs. Dynamic relaxation removes this effect and allows the use of large time-steps. We also noted that Newton convergence is improved with dynamic relaxation.

7 Conclusions

We introduced an alternative method to solve FCC single crystal finite strain plasticity problems. It combines the use of Logarithmic strain additive decomposition, Newton iteration for the plastic strain, a linear solution for the evolution of the hardening variables and an implicit staggered algorithm based on dynamic relaxation. Discretization makes use of an EAS formulation based on the Green-Lagrange strain. Verification tests for mesh size and time step dependences were successfully performed and a polycrystal example from Alankar et al. 2009 was studied for texture evolution. We conclude that the dynamic relaxation is effective in reducing drift caused by the staggered algorithm. Significant savings and computational cost reductions can be achieved and the procedure can be extended to more intricate constitutive laws.

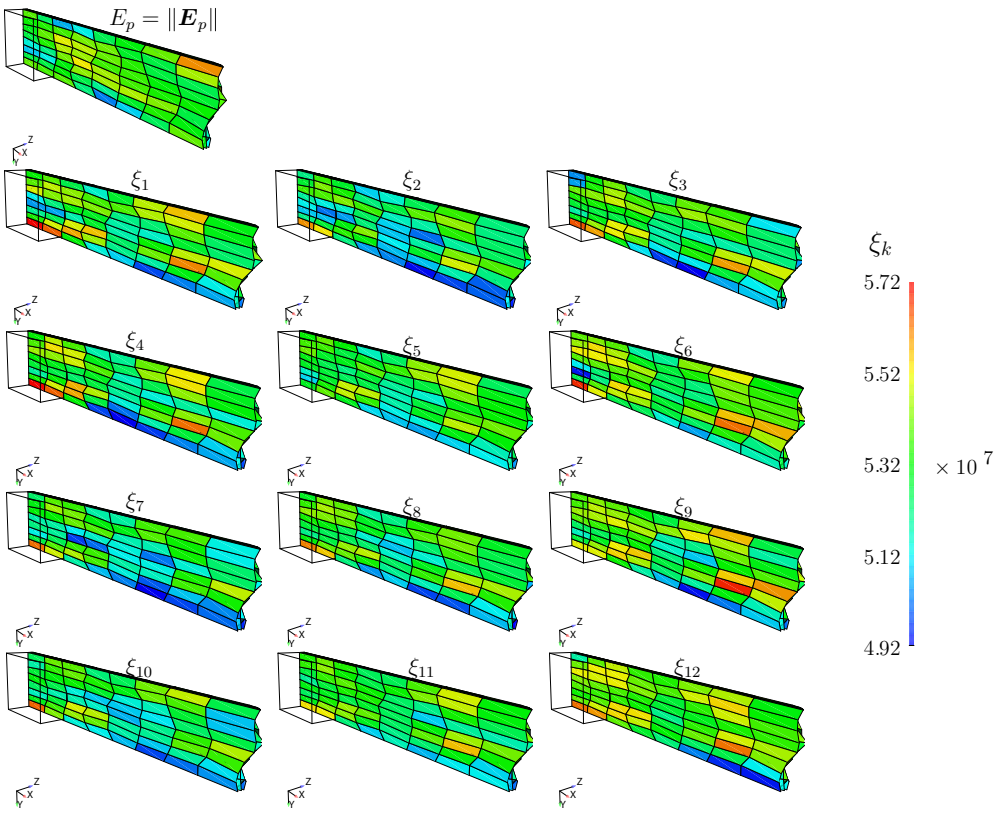

Figure 11 Aluminum polycrystal: distribution of $E_p = \|\boldsymbol{E}_p\|$ and $\xi_1, \ldots, \xi_{12}$ for 80 % compression.

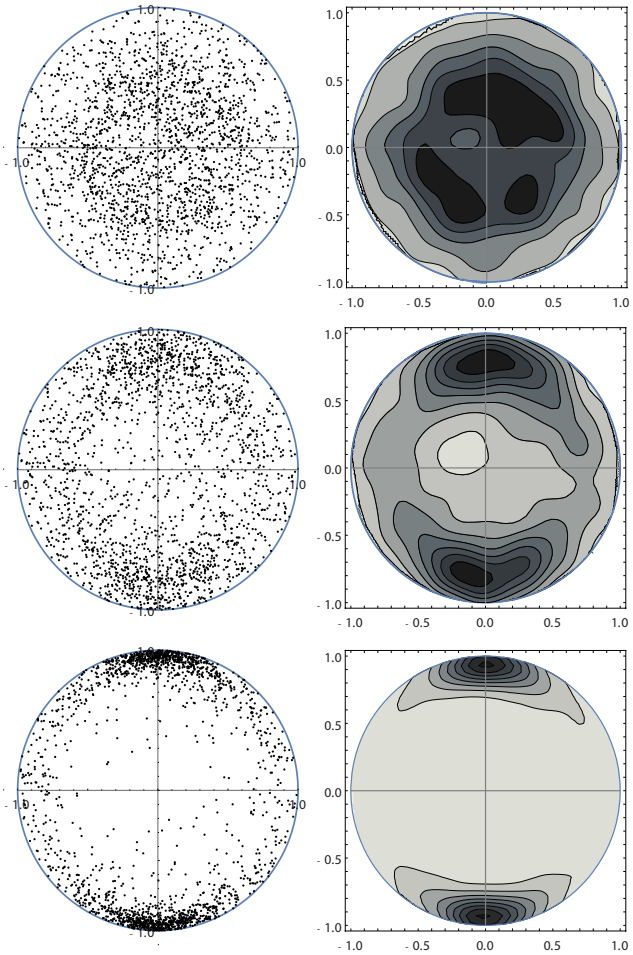

Figure 12 Texture (111) planes, see also (Alankar et al. 2009).

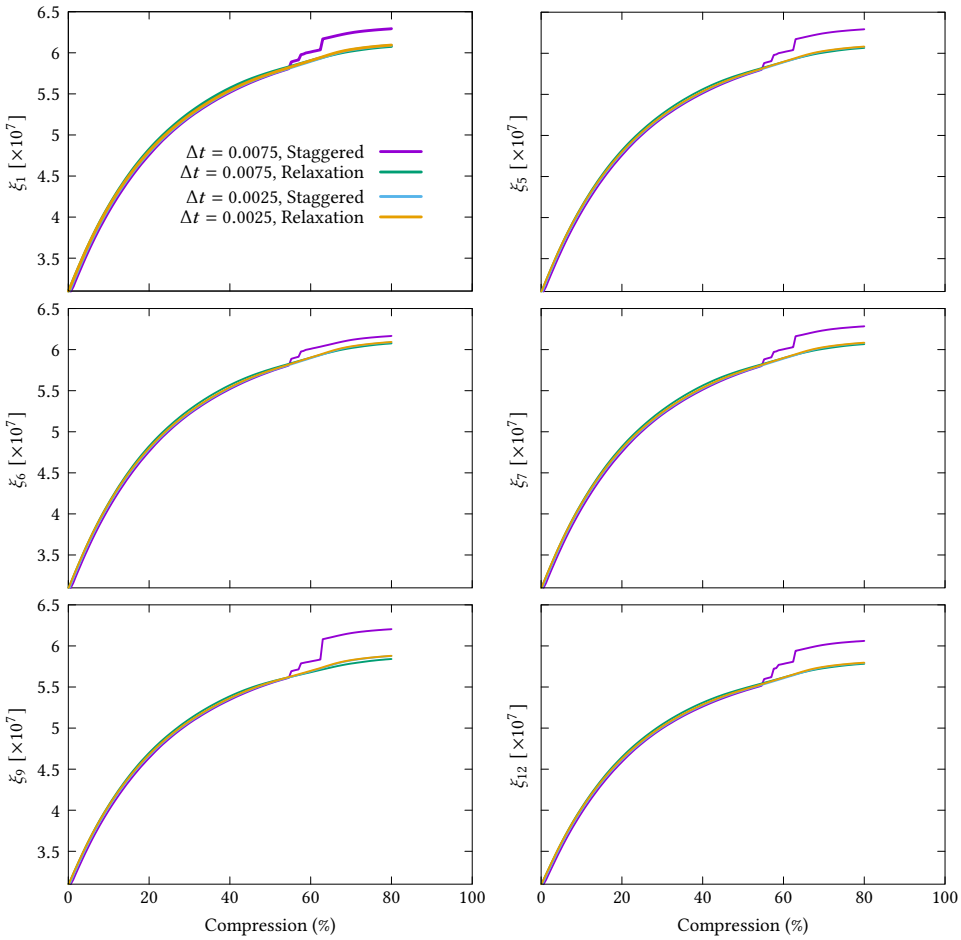

Figure 13 Effect of the algorithm in the evolution of ξ_1, ξ_5, ξ_6, ξ_7, ξ_9 and ξ_{12} at point $(X, Y, Z) = (2 \times 10^{-4}, 0, 0)$. All axis scales are identical.

References

Alankar, A., I. N. Mastorakos, and D. P. Field (2009). A dislocation-density-based 3D crystal plasticity model for pure aluminum. *Acta Materialia* 57(19):5936–5946. [DOI].

Anand, L. (1979). On H. Hencky's approximate strain-energy function for moderate deformations. *Journal of Applied Mechanics* 46(1):78–82. [DOI].

Andelfinger, U. and E. Ramm (1993). EAS-elements for two-dimensional, three-dimensional, plate and shell structures and their equivalence to HR-elements. *International Journal for Numerical Methods in Engineering* 36(8):1311–1337. [DOI].

Areias, P. (2023). *Material logarithmic strain: transformations and tangent modulus.* [URL].

Areias, P. (2024a). *EAS 3D element.* [URL].

Areias, P. (2024b). *Simplas.* Portuguese Software Association (ASSOFT) registry number 2281/D/17. [URL].

Asaro, R. J. (1983). Crystal Plasticity. *Journal of Applied Mechanics* 50(4b):921–934. [DOI].

Asaro, R. and J. Rice (1977). Strain localization in ductile single crystals. *Journal of the Mechanics and Physics of Solids* 25(5):309–338. [DOI], [OA].

Barlat, F., H. Aretz, J. Yoon, M. Karabin, J. Brem, and R. Dick (2005). Linear transformation-based anisotropic yield functions. *International Journal of Plasticity* 21(5):1009–1039. [DOI].

Barlat, F., D. J. Lege, and J. C. Brem (1991). A six-component yield function for anisotropic materials. *International Journal of Plasticity* 7(7):693–712. [DOI].

Bassani, J. and T.-Y. Wu (1991). Latent Hardening in Single Crystals II. Analytical Characterization and Predictions. *Proceedings of the Royal Society of London. Series A: Mathematical and Physical Sciences* 435(1893):21–41. [DOI].

Bažant, Z. (1998). Easy-to-compute tensors with symmetric inverse approximating Hencky finite strain and its rate. *Journal of Engineering Materials and Technology* 120(2):131–136. [DOI].

Belytschko, T., W. Liu, and B. Moran (2000). *Nonlinear Finite Elements for Continua and Structures*. 2nd ed. Wiley. ISBN: 9781118632703.

Bruhns, O. T., H. Xiao, and A. Meyers (2001). Constitutive inequalities for an isotropic elastic strain-energy function based on Hencky's logarithmic strain tensor. *Proceedings of the Royal Society of London. Series A: Mathematical, Physical and Engineering Sciences* 457(2013):2207–2226. [DOI].

Cailletaud, G., O. Diard, F. Feyel, and S. Forest (2003). Computational Crystal Plasticity: From Single Crystal to Homogenized Polycrystals. *Technische Mechanik* 23(2-4):130–145. [OA].

Chang, Y. and R. Asaro (1981). An experimental study of shear localization in aluminum-copper single crystals. *Acta Metallurgica* 29(1):241–257. [DOI].

Degroote, J., R. Haelterman, S. Annerel, P. Bruggeman, and J. Vierendeels (2010). Performance of partitioned procedures in fluid-structure interaction. *Computers & Structures* 88(7-8):446–457. [DOI], [OA].

Erbts, P. and A. Düster (2012). Accelerated staggered coupling schemes for problems of thermoelasticity at finite strains. *Computers & Mathematics with Applications* 64(8):2408–2430. [DOI], [OA].

Felippa, C. A., K. Park, and C. Farhat (2001). Partitioned analysis of coupled mechanical systems. *Computer Methods in Applied Mechanics and Engineering* 190(24-25):3247–3270. [DOI].

Fohrmeister, V., G. Díaz, and J. Mosler (2019). Classic crystal plasticity theory vs crystal plasticity theory based on strong discontinuities—Theoretical and algorithmic aspects. *International Journal for Numerical Methods in Engineering* 117(13):1283–1303. [DOI].

Green, A. E. and P. M. Naghdi (1965). A general theory of an elastic-plastic continuum. *Archive for Rational Mechanics and Analysis* 18(4):251–281. [DOI].

Hughes, T. (2000). *The Finite Element Method. Linear Static and Dynamic Finite Element*. Dover Publications. ISBN: 9780486411811.

Kaiser, T. and A. Menzel (2019). A dislocation density tensor-based crystal plasticity framework. *Journal of the Mechanics and Physics of Solids* 131:276–302. [DOI].

Kasemer, M, G Falkinger, and F Roters (2020). A numerical study of the influence of crystal plasticity modeling parameters on the plastic anisotropy of rolled aluminum sheet. *Modelling and Simulation in Materials Science and Engineering* 28(8):085005. [DOI], [OA].

Kenney, C. and A. J. Laub (1989). Padé error estimates for the logarithm of a matrix. *International Journal of Control* 50(3):707–730. [DOI].

Korelc, J. (2002). Multi-language and multi-environment generation of nonlinear finite element codes. *Engineering with Computers* 18(4):312–327. [DOI].

Kröner, E. (1960). Allgemeine Kontinuumstheorie der Versetzungen und Eigenspannungen. *Archive for Rational Mechanics and Analysis* 4(1):273–334. [DOI].

Küttler, U. and W. A. Wall (2008). Fixed-point fluid-structure interaction solvers with dynamic relaxation. *Computational Mechanics* 43(1):61–72. [DOI].

Le Tallec, P. and J. Mouro (2001). Fluid structure interaction with large structural displacements. *Computer Methods in Applied Mechanics and Engineering* 190(24-25):3039–3067. [DOI].

Lee, E. H. (1969). Elasto-plastic deformation at finite strains. *Journal of Applied Mechanics* 36(1):1–6. [DOI].

Lee, E. H. and D. T. Liu (1967). Finite strain elastic-plastic theory particularly for plane wave analysis. *Journal of Applied Physics* 38(1):19–27. [DOI].

Lehmann, T. (1991). Thermodynamical foundations of large inelastic deformations of solid bodies including damage. *International Journal of Plasticity* 7(1-2):79–98. [DOI].

Matthies, H. G., R. Niekamp, and J. Steindorf (2006). Algorithms for strong coupling procedures. *Computer Methods in Applied Mechanics and Engineering* 195(17-18):2028–2049. [DOI].

Matthies, H. G. and J. Steindorf (2003). Partitioned strong coupling algorithms for fluid-structure interaction. *Computers & Structures* 81(8-11):805–812. [DOI], [OA].

Michler, C., E. van Brummelen, and R. de Borst (2006). Error-amplification analysis of subiteration-preconditioned GMRES for fluid-structure interaction. *Computer Methods in Applied Mechanics and Engineering* 195(17-18):2124–2148. [DOI].

Miehe, C., N. Apel, and M. Lambrecht (2002). Anisotropic additive plasticity in the logarithmic strain space: modular kinematic formulation and. *Computer Methods in Applied Mechanics*

and Engineering 191(47-48):5383–5425. [DOI].

Papadopoulos, P. and J. Lu (1998). A general framework for the numerical solution of problems in finite elasto-plasticity. *Computer Methods in Applied Mechanics and Engineering* 159(1-2):1–18. [DOI].

Papadopoulos, P. and J. Lu (2001). On the formulation and numerical solution of problems in anisotropic finite plasticity. *Computer Methods in Applied Mechanics and Engineering* 190(37-38):4889–4910. [DOI].

Rezaee-Hajidehi, M., K. Tůma, and S. Stupkiewicz (2021). A note on Padé approximants of tensor logarithm with application to Hencky-type hyperelasticity. *Computational Mechanics* 68(3):619–632. [DOI], [OA].

Rice, J. (1971). Inelastic constitutive relations for solids: an internal-variable theory and its application to metal plasticity. *Journal of the Mechanics and Physics of Solids* 19(6):433–455. [DOI].

Romanova, V., R. Balokhonov, O. Zinovieva, D. Lychagin, E. Emelianova, and E. Dymnich (2022). Mechanical Aspects of Nonhomogeneous Deformation of Aluminum Single Crystals under Compression along [100] and [110] Directions. *Metals* 12(3):397. [DOI], [OA].

Roters, F., P. Eisenlohr, L. Hantcherli, D. Tjahjanto, T. Bieler, and D. Raabe (2010). Overview of constitutive laws, kinematics, homogenization and multiscale methods in crystal plasticity finite-element modeling: Theory, experiments, applications. *Acta Materialia* 58(4):1152–1211. [DOI].

Sastre, J., J. Ibáñez, E. Defez, and P. Ruiz (2015). New Scaling-Squaring Taylor Algorithms for Computing the Matrix Exponential. *SIAM Journal on Scientific Computing* 37(1):A439–A455. [DOI], [OA].

Schapira, Y., L. Radtke, S. Kollmannsberger, and A. Düster (2023). Performance of acceleration techniques for staggered phase-field solutions. *Computer Methods in Applied Mechanics and Engineering* 410:116029. [DOI].

Schröder, J., F. Gruttmann, and J. Löblein (2002). A simple orthotropic finite elasto-plasticity based on generalized stress-strain measures. *Computational Mechanics* 30(1):48–64. [DOI].

Shutov, A. and J. Ihlemann (2014). Analysis of some basic approaches to finite strain elasto-plasticity in view of reference change. *International Journal of Plasticity* 63:183–197. [DOI], [ARXIV].

Simo, J. C. and F. Armero (1992). Geometrically non-linear enhanced strain mixed methods and the method of incompatible modes. *International Journal for Numerical Methods in Engineering* 33(7):1413–1449. [DOI].

Simo, J. C. and M. S. Rifai (1990). A class of mixed assumed strain methods and the method of incompatible modes. *International Journal for Numerical Methods in Engineering* 29(8):1595–1638. [DOI].

Simo, J., F Armero, and R. Taylor (1993). Improved versions of assumed strain tri-linear elements for 3D finite deformation problems. *Computer Methods in Applied Mechanics and Engineering* 110(3-4):359–386. [DOI], [OA].

Souza Neto, E. de, D. Perić, and D. Owen (2008). *Computational Methods for Plasticity: Theory and Applications*. Wiley. [DOI].

Wriggers, P. (2008). *Nonlinear Finite Element Methods*. Springer. [DOI].

Xiao, H. (2005). Hencky strain and Hencky model: extending history and ongoing tradition. *Multidiscipline Modeling in Materials and Structures* 1(1):1–52. [DOI].

Zhang, H., M. Diehl, F. Roters, and D. Raabe (2016). A virtual laboratory using high resolution crystal plasticity simulations to determine the initial yield surface for sheet metal forming operations. *International Journal of Plasticity* 80:111–138. [DOI].

Authors' contributions PA carried out the bibliographic review and algorithm implementation, as well as the drafting. CdS organized the bibliography by theme and relative contributions and drew the scientific diagrams. RM assisted with the writing and technical content and NS performed the revisions, provided criticism and further references.

Supplementary Material The results exposed in the present paper can be reproduced using the datasets and software solutions archived at the permalink 10.5281/zenodo.13743459.

Funding The authors acknowledge the Fundação para a Ciência e a Tecnologia (FCT) for its financial support via the project LAETA Base Funding (DOI 10.54499/UIDB/50022/2020).

Competing interests The authors declare that they have no competing interests.

Journal's Note JTCAM remains neutral with regard to the content of the publication and institutional affiliations.